Statistical Model-based Detector via Texture Weight Map: Application in Re-sampling Authentication

Tong Qiao, Ran Shi, Xiangyang Luo, Ming Xu, Ning Zheng, and Yiming Wu

Abstract—The problem of authenticating a re-sampled image has been investigated over many years. However, few current research proposes a statistical model-based test, resulting in that statistical performance of the re-sampling detector could not be completely analyzed. To fill the gap, we utilize a parametric model to expose traces of re-sampling forgery, which is described with the distribution of residual noise. Afterwards, we propose a statistical model describing the residual noise from a re-sampled image. Then the detection problem is cast into the framework of hypothesis testing theory. By considering the image content with designing texture weight map, two types of statistical detectors are established. In an ideal context in which all distribution parameters are perfectly known, the Likelihood Ratio Test (LRT) is presented and its performance is theoretically established. An upper bound of the detection power can be successfully obtained from statistical performance of LRT. For a practical use, when the distribution parameters are not known, a generalized LRT with three different maps based on estimation of parameters is established. Numerical results on simulated data and real natural images highlight the relevance of our proposed approach.

Index Terms—Digital forensics, re-sampling forgery, Gaussian noise model, nuisance parameters, hypothesis testing.

I. Introduction

Due to dramatic development of computer and network technologies, image manipulation has become feasibly and easily with the help of some low-cost photo-editing software. According to the analysis of the website [1], many tampered images have been widely-distributed in our daily life. To re-establish the trustworthiness of digital image, image forensic technique has received an increasing attention from academic community and law enforcement in past two decades. Thus, reliable and robust forensic methods are required to deal with malicious-edited images.

To address the problem of blind image forensics, many methodologies have been proposed and generally categorized into two fields: origin identification and content integrity (see [2] for details). The former research mainly focuses on from what imaging equipment a captured image comes such as algorithms proposed in [3]–[6]. The latter research puts main

Tong Qiao is with School of Cyberspace, Hangzhou Dianzi University, Hangzhou, China; State Key Laboratory of Mathematical Engineering and Advanced Computing, Zhengzhou Science and Technology Institute, Zhengzhou, China; email: tong.qiao@hdu.edu.cn

Ran Shi, who contributed equally to this work as the first author, is with School of Computer Science and Engineering, Nanjing University of Science and Technology, Nanjing, China.

Xiangyang Luo (corresponding author) is with State Key Laboratory of Mathematical Engineering and Advanced Computing, Zhengzhou Science and Technology Institute, Zhengzhou, China; email: xiangyangluo@126.com

Ming Xu, Ning Zheng, and Yiming Wu are with School of Cyberspace, Hangzhou Dianzi University, Hangzhou, China.

focus on the problem of authenticating whether the multimedia (such as image or video) is falsified, such as detection of copy-move (see [7], [8]), splicing (see [9], [10]), re-sampling (see [11], [12]), re-captured audio (see [13]), and even verification of microblog news with typical forged images (see [14]). In addition, the study of identifying multiple image operations for forgery detection is a new research trend (see [15]). In this practical context, we mainly address the problem of how to detect image re-sampling forgery.

Re-sampling is a *post-camera*[1] processing technique. To obtain convincing forged images, a malicious forger most possibly utilizes some geometric operations which require the re-sampling of pixels. Re-sampling falsification often happens together with other forgery techniques. For instance, in order to enhance visual realism, splicing and copy-move forgeries may require geometric transformation such as scaling and/or rotation operations involving pixels re-sampling. Thus, the investigation of re-sampling detection can help forensic researchers explore the operation history of the image under analysis.

In addition, the design of a universal detector (referring to the algorithm capable of detecting many different image manipulations, not one single forgery) increasingly attracts researchers. Although the re-sampling detector cannot be arbitrarily classified into the universal field, detection of re-sampling forgery can help forensic researchers design some universal detectors of unveiling traces of falsified images including splicing, copy-move or other forgery techniques involving pixels re-sampling. Therefore, the research of investigating image re-sampling forgery has been a hot topic in forensic community.

To study the problem of distinguishing between a re-sampled and non-resampled image is what this context mainly focuses on. Forensic methods for exploiting the artifacts of re-sampled images can generally be divided into two following fundamental categories:

1) Unsupervised-based methods investigate the problem of detection mainly relying on the linear correlation left by re-sampling operation. The algorithm in [16] first established a linear predictor, together with Expectation Maximization (EM) algorithm, and unveiled the correlation among neighboring re-sampled pixels. However, the iterative algorithm causes high computation complexity. For simplicity, authors of [17] proposed a re-sampling detector by exploiting the

[1]The term *post-camera* is referred to as the operation after acquiring a digital image. (e.g. re-sampling or re-touching, etc. ...)

second-derivative feature. This method can estimate the interpolation period, yet only applied in the resized images. Towards overcoming the defect of the algorithm in [16], authors of [18] proposed to fix the parametric predictor instead of estimating the interpolation parameters, and design a second-derivative detector. Although the computation efficiency could be improved, the detection accuracy were not able to be guaranteed. By analyzing the variance of the n-th order derivative, it was proposed to expose the trace of a re-sampled image in [19]. However, the proposed algorithm cannot approximate the linear transformation matrix. Afterwards, a series of linear predictors in [20] and a cyclostationary fields-based detector [21] were both proposed to deal with the problem of re-sampling falsification. In addition, based on the set-membership approach, the detector proposed in [22] performed very well with a finite number of observations. In recent research, eigenvalue distribution has been proposed to detect a up-scaled image and estimate its scaling factor (see [23]). Besides, the statistical distance between a down-sampled signal and its original version has been first quantified, and meanwhile the theoretical limits are revealed in [24].

In this category, the proposed algorithms use the specific interpolation feature, and directly establish the corresponding detector. The proposed features possibly cannot be independent of the image content. Therefore, in some cases (e.g. images with many flat regions), some feature-based detectors possibly become invalid. Besides, the problem of how to strike the balance between the computation efficiency and estimation accuracy remains open.

2) Supervised methods in the second category generally work in three steps: features extraction step, training step and testing step. During the features extraction step, all the images are used to extract some features which are expected to be sensitive to the source. One requires to apply the features extraction step on all the images from a training set, that is for which the source is known. In the training step, by using supervised machine learning algorithms, a typical classifier (or re-sampling detector) is established based on the set of the feature vectors. In the testing step, the feature vectors are extracted by means of the same way used in the training step. Then they are put into the trained classifier to achieve the supervised classification. Based on the proposed features such as normalized energy density [12] and together with moment features [25], or second-derivative signals of the image [26], the supervised learning algorithms (such as Support Vector Machine, SVM) were proposed to design re-sampling detectors. Besides, based on the property of blind deconvolution, a hierarchical ensemble detector was proposed for classifying different re-sampling kernels (see [27]).

Although those methods could achieve high true positive rate, supervised statistical learning is time-consuming. Besides, several problems such as the robustness to training and testing set mismatch remain open. In addition, few of both categories investigate the statistical performance of their proposed detectors.

In this context, we design the statistical detector based on the extracted noise modeled by the state-of-the-art distributions. The Likelihood Ratio Test (LRT) with known model parameters is first investigated in detail. Afterwards, we propose to analyze the statistical performance of the LRT. Based on the analysis of its performance, the LRT can help us test the effectiveness of the proposed models. More importantly, we propose three different texture weight maps (or weight value) to deal with selecting residual noise. In virtue of the noise-selected Generalized Likelihood Ratio Test (GLRT) with estimated model parameters, which is not trained previously, the designed re-sampling detector is capable of detecting whether a single inspected image is re-sampled. Hence, the main contributions of this context are the following:

- By using the parametric linear model, this paper successfully extracts the residual noise from the inspected image. Based on the analysis of image content texture, we design three texture weight maps to deal with the problem of selecting residual noise.
- The widely-adopted statistical models, referring to as the Gaussian model (for re-sampled pixels) and Uniform model (for non-resampled pixels), are proposed to describe the distributions of the inspected image. With the aid of designing the texture weight map, it is proposed to select residual noise for constructing the detector.
- In an ideal scenario in which all model parameters are perfectly known, we first design a LRT whose performance is theoretically established. The statistical performance of LRT serves as an upper bound on the detection power for dealing with the problem of discriminating non-resampled and re-sampled images.
- In a practical scenario, it is proposed to design a GLRT with three different texture weight maps. Based on proposed models with estimated parameters, the designed GLRT can effectively authenticate whether the inspected image is re-sampled or not.

This paper is organized as follows. In Section II, we illustrate the principal of image re-sampling, and expose the traces of re-sampling forgery. Based on the proposed linear parametric model, residual noise is successfully extracted and its statistical distribution is explicitly analyzed. In Section III, we mainly study the design of texture weight maps. The LRT and GLRT with texture weight maps are both established in Section IV and V. Section VI presents numerical results of the proposed detectors on simulated and real images. Section VII concludes this paper.

II. EXPOSING TRACES FROM IMAGE RE-SAMPLING

A typical re-sampling procedure is illustrated in Fig. 1. A portion (2×2 block) of an original non-resampled image is first extracted. A subset of pixel values is denoted
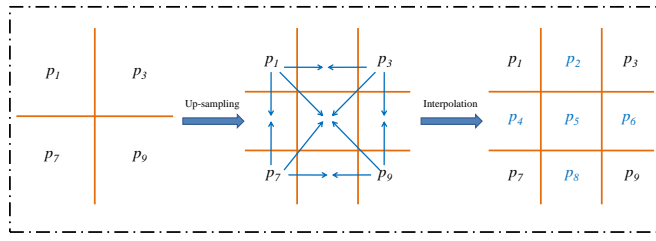
Fig. 1: Illustration of a typical re-sampling operation. Left-most sub-figure: 2×2 original pixels from a non-resampled image; middle sub-figure: some vacant positions appear using up-sampling with $R = 2$; right-most sub-figure: new-generated pixel values (blue) are used to pad the vacant positions.
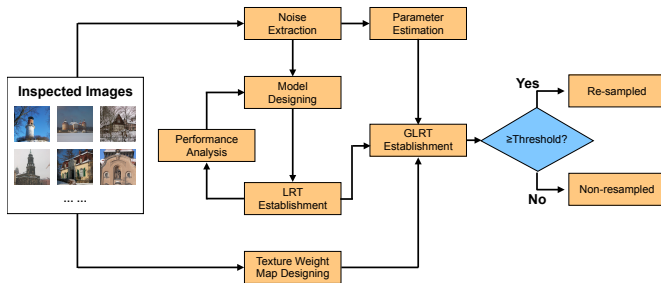

Fig. 2: Framework of establishing the statistical model-based detector with texture weight map for re-sampling authentication.

as $\{P_1, P_3, P_7, P_9\}$. When the non-resampled image is up-sampled with the re-sampling factor $R = 2$, some vacant positions need to be padded by using original neighborhood pixels referring to as the subset of pixels. Based on the interpolation algorithm, each element assigned the corresponding weights from that subset is used to generate the new pixel values. This procedure is defined as linear interpolation. Thus, the new-generated pixel values unavoidably have the correlation information from some of surrounding neighborhood pixel values. For instance, pixel value P_2 benefitted from P_1 and P_3; pixel value P_5 benefitted from all the elements of the subset. By investigating the proposed correlation information existing among the padded pixels, most of prior-art re-sampling detectors are designed.

Let us present the framework of our proposed algorithm (see Fig. 2). First, the residual noise of the inspected image is extracted while designing its texture weight map. Then based on the designed model, the LRT can be smoothly established with known parameters. Through analyzing the performance of the LRT, we can test the effectiveness of the proposed model. In a practical scenario, by estimating model parameters, together with the LRT, the GLRT with texture weight map can be designed. Finally, the threshold of the test discriminates the classification of the inspected image.

A. Fundamental of Re-sampling Detection

Detectors are mainly designed in virtue of traces left by the operation of image re-sampling. One should note that we

refer to traces denoting the unique characteristic of the re-sampled image. First, Let us denote an inspected (authentic or re-sampled) grey-level image as $\mathbf{Z} = \{z_{i,j}\}$ $i \in \{1, ..., I\}$, $j \in \{1, ..., J\}$, where I and J denote the height and the width of the matrix $\mathbf{Z}$. Note that we can straightforwardly obtain the case of color image with three channels. Let us assume the linear correlation among each pixel $z_{i,j}$ and its surrounding neighborhood pixels $z_{i+p,j+q}$, which is formulated by:

$$z_{i,j} = \sum_{p=-f}^{f} \sum_{q=-f}^{f} \lambda_{p,q} z_{i+p,j+q} \qquad (1)$$

where $z_{i,j}$ denotes a pixel intensity. Note that the edge pixels, referring to as the case of $i \in \{0, I\}$ and $j \in \{0, J\}$, of the image are not considered. The indexes $\{i + p, j + q\}$ denote the position of the neighborhood pixel controlled by the distance parameter $f \in \mathbb{N}^+$. For the case of the re-sampled image, the smaller the f is, the stronger the linear correlation existing among pixels is. In our assumption, each pixel $z_{i,j}$ is generated from its surrounding neighborhood pixels whose corresponding weight factors are denoted as $\lambda_{p,q}$ where $\{p, q\}$ denoted as the position information.

We consider two cases: $\mathbf{Z}$ represents an authentic image; $\mathbf{Z}$ is a re-sampled one. In the first case, $z_{i,j}$ has no linear correlation (caused by re-sampling operation, other *in-camera*[2] operations are not considered, such as demosaicing.) with its surrounding pixels $z_{i+p,j+q}$. Therefore, the combination of $z_{i+p,j+q}$ with the weight factor $\lambda_{p,q}$ cannot represent $z_{i,j}$. In the other case, the new-generated pixels $z_{i,j}$ (for instance in Fig. 1, $\{P_2, P_4, P_5, P_6, P_8\}$) can be described by using combination of non-resampled pixels $z_{i+p,j+q}$ (for instance in Fig. 1, $\{P_1, P_3, P_7, P_9\}$) with its corresponding $\lambda_{p,q}$.

Due to utilization of the fixed pattern of re-sampling operation, the pixel values from the re-sampled image appear periodically. In the frequency domain, the periodic characteristic can be exposed in the form of residual noise. Some prior-art detectors authenticate the re-sampled image by analyzing the symmetric bright spots in Fourier domain (see [16], [18], [20]). Nevertheless, towards extracting residual noise is the first step of establishing our proposed detector.

B. Estimate of Residual Noise

In the practical detection, blind forensic investigators do not know any prior information of the inspected image referring to as the re-sampling algorithm. Therefore, it is obligatory to estimate the expectation of each pixel $\widehat{z}_{i,j}$ with the estimated weight factor $\widehat{\lambda}_{p,q}$. For clarity and simplicity, based on the linear correlation (see Eq. (1)), the expected values of column

---

[2]The term *in-camera* is referred to as the whole image acquisition pipeline, which does occur before the image is output from the camera; it is the opposite in that sense to the *post-camera* operations.

pixels $\mathbf{z}_j$ can be described as:

$$\widehat{\mathbf{z}}_j = \mathbf{H} \cdot \widehat{\boldsymbol{\lambda}} \tag{2}$$

$$\text{where} \quad \widehat{\mathbf{z}}_j = \begin{pmatrix} \widehat{z}_{2,j} \\ \widehat{z}_{3,j} \\ \vdots \\ \widehat{z}_{i,j} \\ \vdots \\ \widehat{z}_{I-2,j} \\ \widehat{z}_{I-1,j} \end{pmatrix}, \widehat{\boldsymbol{\lambda}} = \begin{pmatrix} \widehat{\lambda}_{-f,-f} \\ \widehat{\lambda}_{-f+1,-f} \\ \vdots \\ \widehat{\lambda}_{p,q} \\ \vdots \\ \widehat{\lambda}_{f-1,f} \\ \widehat{\lambda}_{f,f} \end{pmatrix}.$$

Then the neighborhood pixel matrix $\mathbf{H}$ is formulated as:

$$\mathbf{H} = \begin{pmatrix} z_{2-f,j-f} & \cdots & z_{2+p,j+q} & \cdots & z_{i+f,j+f} \\ \vdots & \ddots & \vdots & \ddots & \vdots \\ z_{i-f,j-f} & \cdots & z_{i+p,j+q} & \cdots & z_{i+f,j+f} \\ \vdots & \ddots & \vdots & \ddots & \vdots \\ z_{I-1-f,j-f} & \cdots & z_{I-1+p,j+q} & \cdots & z_{I-1+f,j+f} \end{pmatrix},$$

where the expected image $\widehat{\mathbf{Z}} = \{\widehat{\mathbf{z}}_j\}$; j denotes column index. In general, in Eq. (2), the pixel expectation $\widehat{\mathbf{z}}_j$ are unknown. We replace its expectation by $\mathbf{z}_j$. Thus, by using the Least Square algorithm (LS), the expected pixel value can be approximated by:

$$\widehat{\mathbf{z}}_j = \mathbf{H}(\mathbf{H}^{\mathrm{T}}\mathbf{H})^{-1}\mathbf{H}^{\mathrm{T}}\mathbf{z}_j. \tag{3}$$

In fact, for the expected values of each row $\mathbf{z}_i$, the similar result can be expected. For the sake of clarity, let us omit the index $\{i, j\}$ of $z_{i,j}$ in Eq. (1). Thus, the residual noise ω of each pixel can be represented by:

$$\omega = z - \widehat{z}. \tag{4}$$

For clarity, let us describe the image $\mathbf{Z} = \{z\}$ by using the following formulation:

$$z = \mu + \omega. \tag{5}$$

where μ represents the expected value of each pixel z; ω denotes the residual noise. Traditionally, some effective de-noising filters can help us acquire the expected value μ. However, in the procedure of estimation, the estimated errors are not under control. Instead, in this context, based on the LS algorithm, we propose to straightforward extract the residual noise ω using the Eqs. (3) and (4).

In our assumption, the distributions of ω in the two cases (re-sampled and non-resampled) are different. In this present paper, distribution characteristics of ω are the fundamental of establishing our proposed statistical detectors. Therefore, in the following subsection, let us mainly analyze the distribution characteristics of the residual noise.

C. Characteristics of Re-sampled Image

Since our proposed re-sampling detector is established based on the statistical characteristics of the inspected image, let us first investigate the distribution of the residual noise from the re-sampled image. Inspired by our prior algorithm [11], let us assume that the residual noise of the re-sampled image
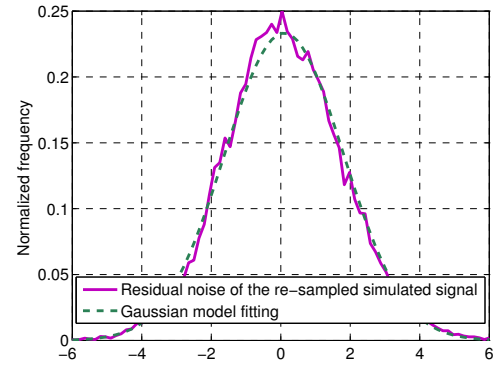

Fig. 3: Illustration of empirical results of the residual noise from re-sampled simulated signal and the theoretical results from its Gaussian model fitting.
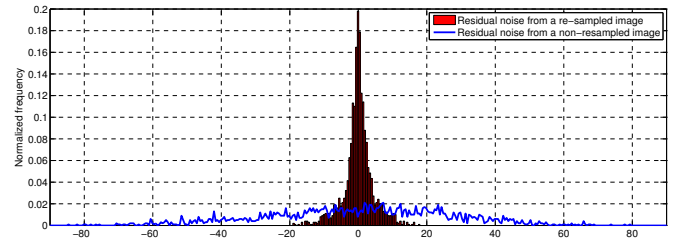

Fig. 4: Illustration of statistical distribution comparison between a non-resampled image (*Baboon*) and its re-sampled version with $R = 1.3$. Let us assume that re-sampled results (red bars) approximately follow the Gaussian distribution; at the given range, non-resampled results (blue curve) are uniformly distributed.
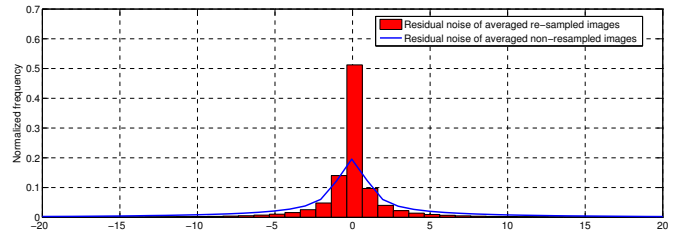

Fig. 5: Illustration of averaged distribution comparison between non-resampled and re-sampled images with $R = 1.3$. The number of tested images (randomly selected from Boss-base [28]) is 200.

approximately follows the Gaussian model. For simplicity and clarity, let us first simulate the residual noise from the non-resampled image by using a set of random variables of 10000 samples. After interpolation, its re-sampled version with 20000 samples is obtained using $R = 2$. Based on the proposed algorithm (see Eq. (4)), the normalized histogram of the extracted residual noise ω is illustrated in Fig. 3. Obviously, the empirical results approximately superpose the theoretical results which are generated using the estimated Gaussian model parameters.

Moreover, to verify the effectiveness of our assumption, it is proposed to illustrate the authentic distributions of the residual noise between a non-resampled image and its re-sampled version. In the stage of noise extraction, we prescribe

f as 1, referring to as the 8 neighbouring pixels for prediction. The normalized histograms of the same portion from the non-resampled and re-sampled image are demonstrated in Fig. 4. After re-sampling forgery, the Uniform distribution of residual noise evolves to the Gaussian model. In this practical context, without any prior information, it is very difficult to model the accurate distribution of a natural (or non-resampled) image. As Fig. 4 illustrates, it hardly holds true that along the whole value range of residual noise, all the random variables generated from the non-resampled image follow the Uniform model. However, at the given range (for instance, from -20 to 20), it is reasonable that portion of random variables approximately follow the proposed Uniform model. In our practical test, the probability of the residual noise falling in that given range is larger than somewhere else.

Still, one might argue that the single image cannot represent all the distributions of tested images. Fig. 5 illustrates the average results of the distribution comparison. In fact, whatever distribution is assumed, when we discuss the average of the distribution, the results (the sum of random variables) always asymptotically follow the Gaussian distribution (if the large number of random variables is given). By observation, the results of the re-sampled images are totally different from that of non-resampled images (even though the noise residual does not follow the Uniform model any more.).

Additionally, due to the inhomogeneity of pixels (or residual noise) of an image, it is hardly possible that one can generalize a reliable and robust model describing the whole image dataset. The forensic researcher mainly cares about the detection performance of the designed classifier. Note that in our practical test, the distinguishable distribution with different model parameters can help us establish the statistical detector, meaning that to some extent the model mismatch between real and assumed data can be tolerable without interfering the final classification. Furthermore, in our evaluation experiment (see Table I), the selection of model (assumed for a non-resampled image) parameters is nearly irrelevant to our final detection. Nevertheless, we have to admit that the proposed Uniform model slightly limits the performance of our designed statistical detector. In both Section IV and V, we will present the details of designing statistical detectors under two hypotheses with different distributions.

Due to the fact that the interpolated pixel obtained from its neighborhood pixels, the periodic characteristic is uncovered unavoidably in the frequency domain. In the prior research of re-sampling detection, some state-of-the-art algorithms ([16], [18], [20] for instance) first gave the probability map, referring to as $\mathbf{P}_{map}$, and then transform $\mathbf{P}_{map}$ from the spatial domain to Fourier domain. By investigating the corresponding frequency spectrum, it was proposed to expose bright spots surrounding the central spot distributed symmetrically in Fourier domain, which was the critical re-sampling artifact of a re-sampled image (see Fig. 6). About the specific calculation of $\mathbf{P}_{map}$ and the frequency spectrum, the reader who has interests refers to [11, Sec. 3.2].

As Fig. 6 illustrates, if the image is re-sampled (see Fig. 6a and 6d), its periodic re-sampling artifact is probably unveiled (see Fig. 6c and 6f). By analyzing the $\mathbf{P}_{map}$ (see Fig. 6b

(a) Re-sampled image (dimension: 256×256) with $R = 1.5$

(b) $\mathbf{P}_{map}$

(c) Frequency spectrum of $\mathbf{P}_{map}$

(d) Re-sampled image (dimension: 461×346) with $R = 0.9$

(e) $\mathbf{P}_{map}$

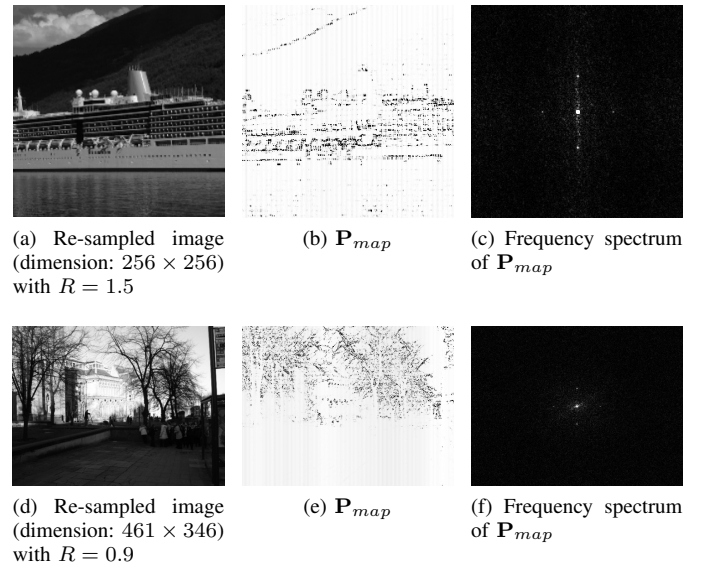(f) Frequency spectrum of $\mathbf{P}_{map}$

Fig. 6: Left-most column: two re-sampled images with different factors; middle column: its corresponding $\mathbf{P}_{map}$; right-most column: frequency spectrum of $\mathbf{P}_{map}$ in Fourier domain.

and 6e), it is observed that the contour profile of the $\mathbf{P}_{map}$ is mainly established using the high texture region of the re-sampled image. By contrast, if the re-sampling is operated in the low texture region of the inspected image, the traces are not obvious. Besides, the increasing number of zero-value residual noise results in the detection error, especially for the model-based detectors.

This phenomenon inspires us to investigate the image content of the inspected image for enhancing the effectiveness of re-sampling detection. Thus, in the following section, it is proposed to mainly investigate the algorithms of image segmentation based on the image texture.

III. DESIGN OF TEXTURE WEIGHT MAP

Let us first analyze the image content referring to as the texture of image from two folds: 1) based on the principle of re-sampling (see Fig. 1); 2) based on the characteristics of $\mathbf{P}_{map}$ (see Fig. 6).

In our method, an assumption is that the variation of the random variable z, referring to the pixel value of the inspected image $\mathbf{Z}$, should be large enough. Otherwise, the expected value $\widehat{z}$ always approximates z. It means that the variance of the residual ω is very small, and meanwhile the distribution of ω (almost equal to zero) becomes uniform. Under the investigation of statistical characteristics from a re-sampled image, this phenomenon is not our expectation. Because it possibly disturbs the accuracy of the proposed model for detecting a re-sampled image. The re-sampled image $\mathbf{Z}$ will probably be mistakenly judged as non-resampled signal, since it hardly holds true that the residual noise ω follows the Gaussian distribution. Besides, even if $\mathbf{Z}$ consists of both a high variation part and a low variation part, the low variation part can still interfere with our judgment. Therefore, our

judgment should mainly depend on the high variation part of the inspected image.

For the case of detecting a re-sampled image, an image can be similarly divided into the smooth region and the texture region. The texture region indicates potential high variation of pixel values. In fact, the $\mathbf{P}_{map}$ is the ratio of probabilities (see [11, Sec. 3.2]), which is controlled by the variance of random variables referring to as the residual noise. With increasing the variance, for the case of the same random variable, the value of $\mathbf{P}_{map}$ is decreasing. Therefore, in the texture region with high variation, the $\mathbf{P}_{map}$ becomes darker than the corresponding region with low variation (see Fig. 6 for instance). In this case, the detailed information of the image is basically described. Moreover, before and after re-sampling forgery, the change of $\mathbf{P}_{map}$ in the texture region is much more obvious. However, the high probability (large value of $\mathbf{P}_{map}$) might not mean that this pixel is not re-sampled. It possibly implies that this pixel is in the smooth region. In order to enhance the true positive rate of re-sampling detection, it is proposed to reduce the interference of the smooth region as much as possible.

Let us generate three typical texture maps with different levels based on a grey-level image (or green channel for the case of color image with three color channels) to deal with the problem of detecting the re-sampled image. For clarity, all the following maps are defined as texture weight map. The specific description is extended as follows:

- Pixel-Level Texture (PLT) map. It is the gradient map to describe the texture information from an inspected image. For each pixel $z_{i,j}$, where $i \in \{1, ..., I\}$ and $j \in \{1, ..., J\}$ respectively denoted as the index of height and width of the image. Its gradient value $\boldsymbol{G} = \{g_{i,j}\}$, referring to as PLT map, is calculated as:

$$g_{i,j} = \sqrt[2]{(z_{i,j} - z_{i+1,j})^2 + (z_{i,j} - z_{i,j+1})^2} \quad (6)$$

- Block-Level Texture (BLT) map. Inherited from the PLT map, we first divide $\boldsymbol{G}$ into non-overlapped gradient blocks. For each block $\boldsymbol{b}_{UV} = \{g_{u,v}\}$, $u \in \{1, ..., U\}$, $v \in \{1, ..., V\}$, the spatial uniformity measure [29] is used to evaluate its texture information. After re-scaling, one pixel $z_{i,j}$ within a block shares this block' s spatial uniformity value $\widetilde{f}_{su}(\boldsymbol{b})$ to indicate the complexity degree of its texture $b_{i,j}$ on the block-level, which is formulated by:

$$\widetilde{f}_{su}(\boldsymbol{b}) = \frac{f_{su}(\boldsymbol{b})}{\max(f_{su}(\boldsymbol{b}))}, \quad (7)$$

where

$$f_{su}(\boldsymbol{b}) = \sqrt[2]{\frac{1}{U \cdot V} \sum_{\{u,v\}} (g_{u,v})^2 - (\frac{1}{U \cdot V} \sum_{\{u,v\}} g_{u,v})^2}$$

where BLT map $\mathbf{B} = \{b_{i,j}\}$ are mapped into each pixel of the inspected image within each gradient block $\boldsymbol{b}$. Without loss of generality, parameters (U, V) control the dimensionality of $\boldsymbol{b}$. Besides, $\max(\cdot)$ denotes the maximum value of spatial uniformity among those of all blocks to reflect the relative texture complexity degree of each image.

- Region-Level Texture (RLT) map. Based on the BLT map, we further segment the BLT map into two regions: high texture region and low texture region, which is defined as:

$$r_{i,j} = \begin{cases} b_{i,j} & \text{if} \quad b_{i,j} > T \\ 0 & \text{otherwise}, \end{cases} \quad (8)$$

where T represents the optimal threshold designed by using the adaptive methodology proposed in [30]. $\mathbf{R} = \{r_{i,j}\}$, denoted as texture map, represents the pixel value on the RLT map. The pixels which can retain their values are treated as locating at the high texture region. Otherwise, their values are set to zero. With this assumption, it is proposed not to consider the pixel value from the low texture region with low variance.

The PLT map measures the contrast between neighbouring pixels. However, it only describes the individual contrast rather than the variation of pixel values within certain region. Therefore, we introduce the BLT map to measure the variation within one block. The high variation indicates the high texture complexity degree of it. Furthermore, in order to extract the texture region and completely eliminate the interference of smooth region, we generate the RLT map by binarizing the BLT map.

In the BLT map, each block's spatial uniformity value is normalized by their maximum value in order to indicate the relative texture complexity degree. Furthermore, we use an adaptive algorithm (see [30]) to determine the threshold in the RLT map. Therefore, we distinguish between the smooth and texture region according to each image's own relative texture distribution by the adaptive methods.

In the practical detection, based on our analysis, the texture region with high variance dominates the detection result, which should be attributed the more weight. On the contrary, the smooth region with low variance probably interfere the detection result, which should be attributed the less weight.

In the following section, it is first proposed to establish the LRT based on the proposed models, meanwhile normalize the expectation and variance of the LRT to the standard Gaussian distribution. Straightforwardly, we theoretically illustrate the statistical performance of the LRT. For the practical detection, by considering three texture weight maps, we will propose the GLRT to deal with the problem of re-sampling detection.

IV. ESTABLISHMENT OF LIKELIHOOD RATIO TEST

A. Problem Statement

The goal of this section is to present the optimal LRT and, more importantly, study its statistical performance; this statistical test is based on the residual noise $\boldsymbol{\Omega} = \{\omega_l\}_{l \in \mathcal{L}}$ extracted from an inspected image in which l denotes the index of each pixel, see Eq. (4) which follows the Gaussian distribution (see Fig. 3) or the Uniform distribution (see Fig. 4). Within the framework of the LRT, hence, the problem of detecting if the inspected image is re-sampled or not, is reduced to a choice between the two following binary

hypotheses defined by $\forall l \in \mathcal{L}$:

$$\begin{cases} \mathcal{H}_0 = \{\omega_l \sim \mathcal{U}(a,b)\}, \\ \mathcal{H}_1 = \{\omega_l \sim \mathcal{N}(0,\sigma^2)\}, \end{cases} \tag{9}$$

where under hypothesis $\mathcal{H}_0$, the residual noise of the non-resampled image follows the Uniform distribution with $\omega_l \in [a,b]$; under hypothesis $\mathcal{H}_1$, the residual noise of the re-sampled image is normally distributed with zero mean and σ^2 variance.

Here, we do not assume all the random variables, saying that residual noise ω_l, are independent and identically distributed across the whole inspected image. Using the algorithm proposed in Section IIb, each partition of clustered ω_l follow the corresponding distribution under $\mathcal{H}_0$ or $\mathcal{H}_1$.

In this context, it is proposed to guarantee a prescribed False Alarm Probability (FAP). Thus, based on the Neyman-Pearson lemma [31, Theorem 3.2.1] that the LRT is optimal in the sense described below, let

$$\mathcal{K}_{\alpha_0} = \{\delta : \mathbb{P}_{\mathcal{H}_0}[\delta(\mathbf{\Omega}) = \mathcal{H}_1] \le \alpha_0\} \tag{10}$$

be the class of tests, with an upper-bounded FAP α_0. Here $\mathbb{P}_{\mathcal{H}_j}[\cdot]$ is the probability under $\mathcal{H}_j, j \in \{0,1\}$. Among all tests in $\mathcal{K}_{\alpha_0}$, our aim is to find a test δ, which maximizes the detection power defined as:

$$\beta_\delta = \mathbb{P}_{\mathcal{H}_1}[\delta(\mathbf{\Omega}) = \mathcal{H}_1]. \tag{11}$$

In the following subsection, the LRT is first described in detail and then its statistical performance is analytically established.

B. Optimal Detection Framework

We assume that all model parameters are known in advance, relying on the Neyman-Pearson Lemma [31, theorem 3.2.1], the LRT is the most powerful test in $\mathcal{K}_{\alpha_0}$ (10), written by:

$$\delta(\mathbf{\Omega}) = \begin{cases} \mathcal{H}_0 & \text{if } \Lambda(\mathbf{\Omega}) = \sum_{l \in \mathcal{L}} \Lambda(\omega_l) < \tau, \\ \mathcal{H}_1 & \text{if } \Lambda(\mathbf{\Omega}) = \sum_{l \in \mathcal{L}} \Lambda(\omega_l) \ge \tau, \end{cases} \tag{12}$$

where the decision threshold τ is the solution of Eq. $\mathbb{P}_{\mathcal{H}_0}[\Lambda(\mathbf{\Omega}) \ge \tau] = \alpha_0$, to ensure that the FAP of the LRT equals α_0. In virtue of the proposed distribution under two hypotheses, let us define statistical parameters $\boldsymbol{\theta}_0 = (a,b)$ and $\boldsymbol{\theta}_1 = (0,\sigma^2)$. Then the probability density function (pdf) is given as: $\mathcal{P}_{\boldsymbol{\theta}_0}$ and $\mathcal{P}_{\boldsymbol{\theta}_1}$. Thus one can obtain the log Likelihood Ratio (LR) for one observation given by:

$$\Lambda(\omega_l) = \log \frac{\mathcal{P}_{\boldsymbol{\theta}_1}[\omega_l]}{\mathcal{P}_{\boldsymbol{\theta}_0}[\omega_l]}. \tag{13}$$

C. Statistical Performance of LRT

By investigating the proposed LRT easily, it is proposed to use some asymptotic theorems, which are relevant in this context as the number of residual noise is chosen very large. In this context, since the distribution of a re-sampled image can be modeled using Gaussian distribution, more accurate than the Uniform model of a non-resampled image. Therefore, once the moments of the LR have been calculated analytically under

hypothesis $\mathcal{H}_1$, one can normalize $\Lambda'(\mathbf{\Omega})$ under hypothesis $\mathcal{H}_1$. First, let us denote $E_{\mathcal{H}_1}(\Lambda(\omega_l))$ and $V_{\mathcal{H}_1}(\Lambda(\omega_l))$ the expectation and the variance of the LR $\Lambda(\omega_l)$ under hypothesis $\mathcal{H}_1$. The Lindeberg's central limit theorem (CLT) [31, theorem 11.2.5] states that since the number of residual noise tends to infinity it holds true that:

$$\Lambda'(\mathbf{\Omega}) = \frac{\sum_{l \in \mathcal{L}} (\Lambda(\omega_l) - E_{\mathcal{H}_1}(\Lambda(\omega_l)))}{\left(\sum_{l \in \mathcal{L}} V_{\mathcal{H}_1}(\Lambda(\omega_l))\right)^{1/2}} \xrightarrow{D} \mathcal{N}(0,1), \tag{14}$$

where $\xrightarrow{D}$ represents the convergence in distribution and the normalized LR $\Lambda'(\mathbf{\Omega})$ can asymptotically follows the standard normal distribution $\mathcal{N}(0,1)$ with zero mean and unit variance. This theorem is of crucial interest to establish the statistical properties of the proposed tests [32]–[34].

Let us straightforwardly define the normalized LRT with $\Lambda'(\mathbf{\Omega})$ by:

$$\delta'(\mathbf{\Omega}) = \begin{cases} \mathcal{H}_0 & \text{if } \Lambda'(\mathbf{\Omega}) < \tau' \\ \mathcal{H}_1 & \text{if } \Lambda'(\mathbf{\Omega}) \ge \tau'. \end{cases} \tag{15}$$

Thus, let us establish the statistical properties of the LRT (15).

Proposition 1. *Assuming that for the problem of classifying between non-resampled and re-sampled images within the binary hypotheses* (15), *in which both model parameters* $\boldsymbol{\theta}_0$ *and* $\boldsymbol{\theta}_1$ *are known, then for any* $\alpha_0 \in (0,1)$ *the decision threshold:*

$$\tau' = \left(\sqrt{\frac{v_0}{v_1}}\Phi^{-1}(1-\alpha_0) + \frac{\mu_0 - \mu_1}{\sqrt{v_1}}\right), \tag{16}$$

where

$$\mu_j = \sum_{l \in \mathcal{L}} E_{\mathcal{H}_j}(\Lambda(\omega_l)) \tag{17}$$

$$v_j = \sum_{l \in \mathcal{L}} V_{\mathcal{H}_j}(\Lambda(\omega_l)), j = \{0,1\}. \tag{18}$$

guarantees that the LRT is in the class $\mathcal{K}_{\alpha_0}$, *see* (10). *Here* Φ *and* Φ^{-1} *respectively represent the cumulative distribution function (cdf) of the standard normal distribution and its inverse.*

Proposition 2. *Assuming that for the problem of classifying between non-resampled and re-sampled images within the binary hypotheses* (15), *where both model parameters* $\boldsymbol{\theta}_0$ *and* $\boldsymbol{\theta}_1$ *are known, for any decision threshold* τ', *the power (or true positive rate) function associated with the proposed test* δ' *is given by:*

$$\beta_{\delta'} = 1 - \Phi(\tau'), \tag{19}$$

The main advantage of normalizing the LR can be emphasized in Eqs. (16) and (19): regardless of any model parameters, it allows us to set any threshold that guarantees a FAP independently. In addition, the specific calculation of Eqs. (17) and (18) is extended in Appendix A.

V. Design of Generalized Likelihood Ratio Test

The framework of our proposed statistical detection based on hypothesis testing theory has been stated assuming that all the model parameters are previously known for each residual noise. To solve the problem of practical detection, let us establish a GLRT. A usually-adopted solution is to replace the unknown parameters using their ML estimation. Due to the pixel intensity of a 8-bit grey-level image (for the case of three color channel image, only one channel is used for testing.) ranging from 0 to 255, residual noise (difference between the pixel's intensity and its expectation value) falls in the range from -255 to 255. For simplicity, in the practical context, one can assume the parameters $\boldsymbol{\theta}_0$ has been known. To analyze the parameters $\boldsymbol{\theta}_1$ of the distribution models (see Section IIb), only one parameter, referring to as the variance σ^2, has to be estimated.

First, all the residual noise are successfully estimated using the algorithm discussed in Section IIb. Afterwards, it is proposed to segment all the residual noise $\{\omega_l\}_{l\in\mathcal{L}}$ into K non-overlapped subsets, consisting of I residual noise in each subset $\boldsymbol{\omega}_k$. Thus, the residual noise is re-defined as $\boldsymbol{\Omega} = \{\omega_{k,i}\}$, $k \in \{1, ..., K\}$, $i \in \{1, ..., I\}$.

In virtue of the discussion in Section III, the main strength of our proposed GLRT is to adaptively select the residual noise based on the proposed texture weight map, which is used for designing the GLRT. Thus, the proposed statistical test is defined as:

$$\widehat{\delta}(\boldsymbol{\Omega}) = \begin{cases} \mathcal{H}_0 \ \ \text{if } \widehat{\Lambda}(\boldsymbol{\Omega}) = \sum_{k=1}^{K}\sum_{i=1}^{I} \widehat{\Lambda}_{ns}(\omega_{k,i}) < \widehat{\tau}_1, \\ \mathcal{H}_1 \ \ \text{if } \widehat{\Lambda}(\boldsymbol{\Omega}) = \sum_{k=1}^{K}\sum_{i=1}^{I} \widehat{\Lambda}_{ns}(\omega_{k,i}) \geq \widehat{\tau}_1, \end{cases} \quad (20)$$

where, again to ensure $\widehat{\delta}(\boldsymbol{\Omega})$ to be in the class $\mathcal{K}_{\alpha_0}$, the solution of the equation $\mathbb{P}_{\mathcal{H}_0}[\widehat{\Lambda}(\boldsymbol{\Omega}) \geq \widehat{\tau}_1] = \alpha_0$. The noise-selected decision statistic is formulated as:

$$\widehat{\Lambda}_{ns}(\omega_{k,i}) = \widehat{\Lambda}(\omega_{k,i}) \cdot w_{k,i} \quad (21)$$

where the log Generalized Likelihood Ratio (GLR) $\widehat{\Lambda}(\omega_{k,i})$ of a single residual noise is given and a weight factor $w_{k,i}$, representing texture weight map, selects the residual noise. Immediately, let us define the GLR as:

$$\widehat{\Lambda}(\omega_{k,i}) = \log \frac{\mathcal{P}_{\widehat{\boldsymbol{\theta}}_1}[\omega_{k,i}]}{\mathcal{P}_{\boldsymbol{\theta}_0}[\omega_{k,i}]}, \quad (22)$$

where the unknown parameter $\widehat{\boldsymbol{\theta}}_1 = (0, \widehat{\sigma}_k^2)$ can be estimated using ML algorithm[3]:

$$\widehat{\sigma}_k^2 = \frac{\sum_{i=1}^{I}(\omega_{k,i} - \frac{1}{I}\sum_{i=1}^{I}\omega_{k,i})^2}{I - 1}. \quad (23)$$

Next, it is proposed to study the $w_{k,i}$. Different from the traditional GLRT assigning a uniform weight to each residual noise, our GLRT weights the residual noise according to the texture weight map. As discussed before, this strategy can promote our GLRT more depending on the residual noise

[3]It is assumed that in each subset $\boldsymbol{\omega}_k = \{\omega_{k,1}, ..., \omega_{k,I}\}$, all the random variable are i.i.d.

with a high variation. In Section III, we have discussed three possible solutions of dealing with the texture weight map, namely PLT, BLT and RLT (see Eqs. (6), (7) and (8)). When detecting a re-sampled image, the forensic analyst can select one of them to design the GLRT. The weight of the residual noise is indexed by its corresponding location in the selected texture weight map.

For the whole image, let us normalize the decision statistic $\widehat{\Lambda}(\boldsymbol{\Omega})$ under hypothesis $\mathcal{H}_1$. Similar to the calculation of LRT, its expectation and variance is formulated by:

$$\mu_j^\star = \sum_{k=1}^{K}\sum_{i=1}^{I} E_{\mathcal{H}_j}(\widehat{\Lambda}_{ns}(\omega_{k,i})) \quad (24)$$

$$v_j^\star = \sum_{k=1}^{K}\sum_{i=1}^{I} V_{\mathcal{H}_j}(\widehat{\Lambda}_{ns}(\omega_{k,i})), j=\{0,1\}. \quad (25)$$

Thus, the normalized GLR $\widehat{\Lambda}^\star(\boldsymbol{\Omega})$ can be obtained by:

$$\widehat{\Lambda}^\star(\boldsymbol{\Omega}) = \frac{\widehat{\Lambda}(\boldsymbol{\Omega}) - \mu_1^\star}{\sqrt{v_1^\star}}. \quad (26)$$

The corresponding statistical test $\widehat{\delta}^\star(\boldsymbol{\Omega})$ can be re-formulated by:

$$\widehat{\delta}^\star(\boldsymbol{\Omega}) = \begin{cases} \mathcal{H}_0 \ \ \text{if } \widehat{\Lambda}^\star(\boldsymbol{\Omega}) < \widehat{\tau}_1^\star, \\ \mathcal{H}_1 \ \ \text{if } \widehat{\Lambda}^\star(\boldsymbol{\Omega}) \geq \widehat{\tau}_1^\star. \end{cases} \quad (27)$$

Proposition 3. *Assuming that for the problem of classifying between non-resampled and re-sampled images within the binary hypotheses* (27), *in which both model parameters $\boldsymbol{\theta}_0$ and $\boldsymbol{\theta}_1$ are successfully estimated, then for any $\alpha_0 \in (0,1)$ the decision threshold is given by:*

$$\widehat{\tau}_1^\star = \left(\sqrt{\frac{v_0^\star}{v_1^\star}} \Phi^{-1}(1 - \alpha_0) + \frac{\mu_0^\star - \mu_1^\star}{\sqrt{v_1^\star}} \right), \quad (28)$$

Proposition 4. *Assuming that for the problem of classifying between non-resampled and re-sampled images within the binary hypotheses* (27), *where both model parameters $\boldsymbol{\theta}_0$ and $\boldsymbol{\theta}_1$ are successfully estimated, for any decision threshold $\widehat{\tau}_1^\star$, the power function associated with the proposed test $\widehat{\delta}^\star$ is given by:*

$$\beta_{\widehat{\delta}^\star} = 1 - \Phi(\widehat{\tau}_1^\star). \quad (29)$$

The proposed GLRT $\widehat{\delta}^\star$ has its main advantages: 1) we can easily establish its statistical performance and, hence, obtain the decision threshold guaranteeing a prescribed FAP along with the ensuing power function and 2) due to the normalization the decision threshold $\widehat{\tau}_1^\star$ only depends on the prescribed FAP α_0.

VI. Numerical Experiments

A. Results on Simulated Images for Re-sampling Detection

To verify the sharpness of our proposed algorithm under the framework of hypothesis testing theory, we use the Monte-Carlo simulation to deal with simulated data. With the establishment of performance analysis presented in Section IV, the effectiveness of the LRT can be tested. The model parameters $\boldsymbol{\theta}_0$ of non-resampled image are characterized by

$(a, b) = (-3.2, 3.2)$ empirically estimated[4] by using a large scale of non-resampled images from Bossbase dataset [28]; the model parameters $\boldsymbol{\theta}_1$ of re-sampled image are empirically characterized by $(0, \sigma^2) = (0, 0.9)$ estimated from the same dataset. To this end, our proposed simulation reduces to a very simple test classifying between the Uniform-distributed and the Gaussian-distributed random variables both with known parameters. When all the required model parameters have been detailed, one can immediately generate two sets of random variables in virtue of repeating 10000 simulation with both model parameters $\boldsymbol{\theta}_0$ and $\boldsymbol{\theta}_1$.

The first set consists of 10000 non-resampled simulated images with 5000 random variables; the other set includes 10000 re-sampled simulated images with 5000 random variables. It makes sense that when investigating the problem of classification based on hypothesis testing theory, one has to keep the same number of inspected variables (such as images) under two hypotheses.

In the first comparison experiment, it is proposed to illustrate the empirical and theoretical distributions under two hypotheses. Empirical results (statistical histogram) can be obtained from simulated data; theoretical results with known parameters are computed based on the pdf of the Gaussian distribution; theoretical results with estimated parameters are also computed based on the pdf, but using the estimated parameters from simulated data. The rule of normalization refers to as Eq. (14). As Fig. 7a presents, under hypothesis $\mathcal{H}_0$, the normalized LR $\Lambda'(\boldsymbol{\Omega})$ approximately follows the Gaussian distribution with expectation $\frac{\mu_0 - \mu_1}{\sqrt{v_1}}$ and variance $\frac{v_0}{v_1}$. Then under hypothesis $\mathcal{H}_1$, Fig. 7b illustrates that the normalized LR $\Lambda'(\boldsymbol{\Omega})$ approximately follows the standard normal distribution. Nearly overlapped curves between empirical and theoretical results directly verify the accuracy and correctness of the established statistical performance. Note that the empirical results under hypothesis $\mathcal{H}_0$ cannot perform very well as under hypothesis $\mathcal{H}_1$. Because the normalization is operated using model parameters under $\mathcal{H}_1$. Besides, our proposed Uniform model for a non-resampled image cannot perform as well as the Gaussian model for a re-sampled image.

Another contribution of this present paper is to design a statistical test with warranting the prescribed FAP. Thus, it is proposed to verify the theoretically established propositions (see Props. 1 and 2). In virtue of the normalization rule under hypothesis $\mathcal{H}_0$, it is very easy to test the effectiveness of the empirical and theoretical FAP α_0, which has been studied in our prior research (see [4], [5], [34] for details). However, in this context, the model performs better under hypothesis $\mathcal{H}_1$ than hypothesis $\mathcal{H}_0$. Therefore, one can use an alternative solution to deal with the propositions. As Fig. 8 illustrates, with increasing the value of the threshold τ', the empirical and theoretical results of detection power $\beta_{\tau'}$ are perfectly overlapped. The well-performed results directly verify our solid Prop. 2. Instead of FAP α_0, the false positive rate α_1 both from empirical and theoretical data also follows the same trajectory. The desirable results indirectly verify our

<hr/>

[4]In our simulation, the selection of (a, b) is not unique; for instance, the wide range (-20, 20) can also be selected. In our practical detection, the detection performance hardly relies on (a, b) (see Table I).
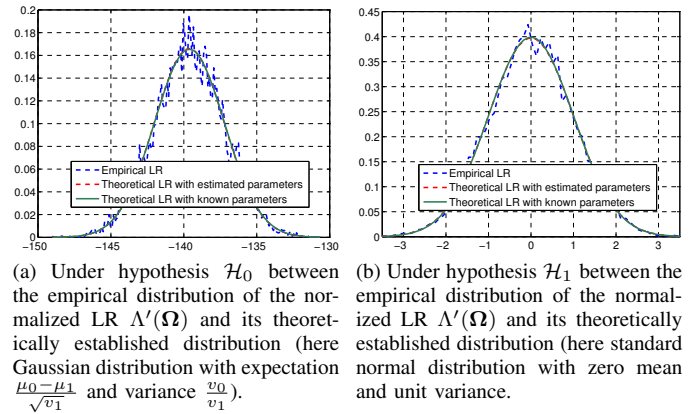

(a) Under hypothesis $\mathcal{H}_0$ between the empirical distribution of the normalized LR $\Lambda'(\boldsymbol{\Omega})$ and its theoretically established distribution (here Gaussian distribution with expectation $\frac{\mu_0 - \mu_1}{\sqrt{v_1}}$ and variance $\frac{v_0}{v_1}$).

(b) Under hypothesis $\mathcal{H}_1$ between the empirical distribution of the normalized LR $\Lambda'(\boldsymbol{\Omega})$ and its theoretically established distribution (here standard normal distribution with zero mean and unit variance.

Fig. 7: Comparison between empirical and theoretical distribution of the normalized LR $\Lambda'(\boldsymbol{\Omega})$.
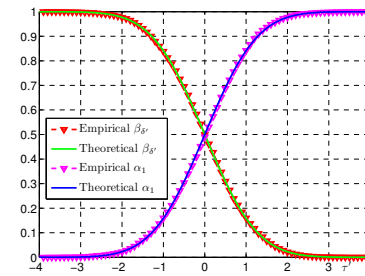

Fig. 8: Comparison between the theoretical detection power $\beta_{\delta'}$ (see Eq. (19)) of the test $\delta'(\boldsymbol{\Omega})$ (see Eq. (15)) and its empirical results; theoretical false positive rate $\alpha_1 = 1 - \beta_{\delta'}$ and its empirical results, both plotted as a function of the threshold τ'.

proposed Prop. 1. Obviously, when the value of threshold τ' is set around -2, the detection power $\beta_{\tau'}$ nearly achieves the maximum with limiting the minimum false positive rate α_1.

To further verify the effectiveness of our proposed algorithm on the simulated data, let us compare our algorithm to the prior art, namely the set-membership technique (see [22] for details). For fair comparison, it is proposed to establish the same testing dataset as that of [22], involving the non-resampled 8-bit signal with the Uniform distribution, and the re-sampled signal with R ranging from 0.6 to 2. Besides, the dimension of the re-sampled signal is set to 512, 256, and 128. We evaluate our detection performance using the metric: *Accuracy*, which is defined as the percentage of correctly classified samples among the total number of samples. As Fig. 9 illustrates, when the number of observations equals to 512 or 256, regardless of the re-sampling factors, our proposed detector achieves the optimal detection results. In the case that 128 observations are used for detection, the performance of our detector is slightly worse than the method of [22] with $R \in [1.1, 1.6]$. However, when $R > 1.7$ or $R < 1$, our detector outperforms that of [22]. In fact, when the number of observations is decreased, such as 128 for instance, the performance of our proposed algorithm is slightly degraded. It reflects that the enough amount of data is the prerequisite of good performance by using our statistical detector.
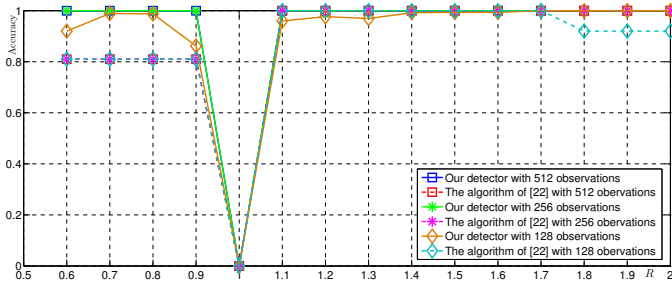
Fig. 9: Illustration of detection performance; the results are obtained by using our proposed detector with different numbers of observations, and also comparison with the prior-art algorithm [22]; the re-sampling factor R ranges from 0.6 to 2 with step sizes 0.1.

B. Results on Real Images for Re-sampling Detection

In this context, our major contribution is to establish the statistical practical detector with estimated parameters for authenticating re-sampled images. To verify the effectiveness of our proposed GLRT in the practical detection, let us establish the original non-resampled image dataset. First all the images of Ucid dataset (see [35]) with dimension 512×382 are used to test re-sampling forgery, in which all 1338 color images with uncompressed format are cropped into small size with $R = 0.5$. We use cropped images in order to decrease that disturbance caused by the fact that post-processing such as color filter array interpolation unavoidably introduces some re-sampling traces. Moreover, in the procedure of capturing an image, the green channel generally conserves more original information (instead of estimating missing pixel values by interpolation) than two other channels. Therefore, all the cropped color images are converted to grey-level images by only selecting the green channel of a color image. Finally, the original non-resampled image dataset, namely *Org_D_1.0*, is successfully established.

For simplicity, in this context, we evaluate the detector performance using one often-adopted re-sampling algorithm, referring to as *bilinear* re-sampling algorithm. Note that except for the results of Table II and III, all the remaining experimental results are acquired by using *bilinear* interpolation. In virtue of dataset *Org_D_1.0*, re-sampled image datasets *Re_D_X* are smoothly established including 1338 grey-level images with different re-sampling factor R. One should note that in "*Re_D_X*", "Re" denotes "Re-sampled"; "D" denotes "Dateset"; "X" denotes the value of re-sampling factor.

1) Selection of Optimal Parameter θ_0: Let us first evaluate the effectiveness of the proposed model for a non-resampled image to the detection performance. Due to the assumed Uniform model with $\theta_0 = (a, b)$, it is proposed to give the empirical results by adopting different θ_0. Meanwhile, three texture maps are used. The test dataset involves *Org_D_1.0* and *Re_D_1.2*. As Table I illustrates, when extending the range of the prescribed θ_0, the performance of detector nearly remains same, which empirically verifies that the performance of our statistical detector is nearly independent of θ_0.

2) Performance over Texture Weight Map (TWM): In our experiments, let us use the Receiver Operating Characteristic
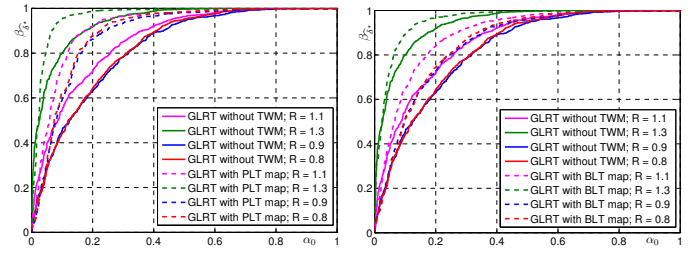
(a) ROC curves from the GLRT with/without PLT map.

(b) ROC curves from the GLRT with/without BLT map.
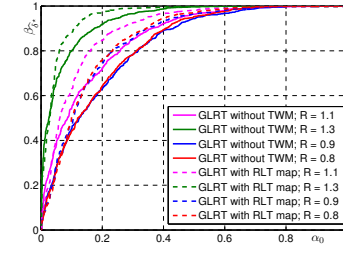
(c) ROC curves from the GLRT with/without RLT map.

Fig. 10: Illustration of detection performance; the results (dotted lines) are obtained by using three texture weight maps: PLT, BLT, and RLT; the re-sampling factor R equals 0.8, 0.9, 1.1, and 1.3 (results from the same test dataset are demonstrated using the same color). To verify the improvement of our proposed algorithm, the results (solid lines) of GLRTs without texture weight map (TWM) are also illustrated.

TABLE I: Detection performance (Area Under Curve, AUC) comparison. The designed GLRT with three texture weight maps, referring to as PLT, BLT, and RLT.

Parameter θ_0	PLT	BLT	RLT
[-1, 1]	0.9721	0.9632	0.9629
[-4, 4]	0.9721	0.9632	0.9629
[-10,10]	0.9721	0.9632	0.9628
[-20, 20]	0.9721	0.9632	0.9628
[-80, 80]	0.9721	0.9632	0.9628
[-255, 255]	0.9721	0.9632	0.9628

(ROC) curve to measure the detection performance of our proposed detectors. In this test, dataset *Org_D_1.0* is respectively coupled with *Re_D_X* to establish each test dataset. In the test dataset, half images are non-resampled; half images are re-sampled. For instance, when the proposed detector is trying to classify between non-resampled and re-sampled images with $R = 1.1$, then we establish the test dataset including *Org_D_1.0* and *Re_D_1.1*. Besides, to verify the effectiveness of texture weight maps, it is proposed to compare the results between the GLRT with three maps and the GLRT without TWM.

First, it is proposed to use the GLRT with PLT map for detecting re-sampling images. As Fig. 10a illustrates, the performance of the GLRT with PLT map is remarkably enhanced in comparison to the GLRT without TWM. When $R > 1$, the number of the padded pixels is larger than that of the missing

pixels; when $R < 1$, the number of the padded pixels is smaller than that of the missing pixels. Besides, down-sampling more or less impairs the structure of the inspected image. Hence, the performance of the proposed detector from $R < 1$ is worse than $R > 1$. Nevertheless, PLT map indeed helps the GLRT improve the detection power for both up-sampling and down-sampling. In addition, when $R > 1$, the proposed detector performs better and better by increasing R. Due to the larger value of R, the more correlated information is introduced. That means the accuracy of the detector is higher.

Subsequently, let us test the performance of the other two GLRTs with BLT and RLT map. When BLT or RLT map is adopted by designing the GLRT, we empirically set the dimension parameter $(U = 15, V = 15)$ of each gradient block (see Eq. (7)). It is proposed to use the same test dataset as the experiments from Fig. 10a. Compared with the GLRT without TWM, both of the GLRTs with BLT and RLT map can improve the detection accuracy (see Fig. 10b and 10c). Therefore, our proposed three texture weight maps are indeed capable of improving the detection power. In the following experiments, it is proposed to specifically analyze the capabilities of three texture weight maps.

Furthermore, let us evaluate the performance of our detector with more different re-sampling factors (a step size of 0.2, ranging from 0.5 to 1.7). Fig. 11 illustrates the AUC results of the GLRTs using three maps, in comparison with the GLRT without TWM. Obviously, our proposed detector with PLT map performs better than the others.

Possibly, the GLRT with PLT map is our optimal option when detecting re-sampling images (see Fig. 10 and 11 for comparison). However, we propose to challenge that conjecture. It is proposed to re-inspect the performance of three texture maps using a new dataset such as Bossbase dataset [28]. Similarly, we randomly select 1000 images as our original non-resampled images while comparing the performance of the GLRT with three texture maps. Fig. 12 illustrates the experimental results. At the low FAP, such as $\alpha_0 \in [0.08\ 0.2]$, the GLRT with RLT slightly performs better that two other GLRTs.

By analyzing the performances of different texture maps over two datasets, we observe that different texture maps are proper to different image contents. For Ucid dataset, many images consist of several smooth regions, only the boundary information can be used to aid our detection. Therefore, the pixel-wise PLT map can achieve better performance, and the performance of BLT and RLT maps are worse due to the error weights induced by the block effect. Conversely, there are more images with rich texture regions in Bossbase dataset. Thus, the block-based map, referring to as BLT or RLT, can achieve better performance because they can well describe the texture information and estimate the corresponding weights.

During residual noise extraction, it is proposed to use different block-wise solutions. In the first group of experiments (see Fig. 10 and 12), we adopt 3×3 or first-order block, referring to as the neighbouring 8 candidate pixels. If we use 5×5 or second-order block, 16 pixels can be used to extract residual noise. In this scenario, more correlated information can be utilized resulting in more accurate estimated noise following
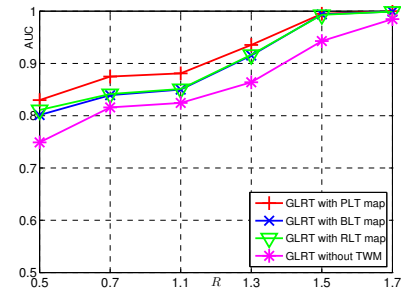

Fig. 11: Illustration of detection power of the GLRT with three maps, and its performance without texture weight map (TWM); the test dataset consists of all non-resampled images from Ucid dataset and its re-sampled version with $R \in [0.5\ 1.7]$.
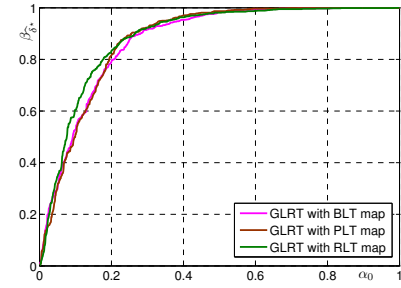

Fig. 12: Illustration of detection power of the GLRT with three maps; the test dataset consists of 1000 randomly-selected non-resampled images from Bossbase dataset and its re-sampled version with $R = 1.1$.

our proposed Gaussian model. In fact, Fig. 13 verifies our assumption. With enlarging the size of pixel neighborhood, the detection accuracy increases at the given FAP. However, if we continuously increase the size of the pixel neighborhood such as third-order neighborhood with 7×7 pixels, the detection power cannot be enhanced. Because some uncorrelated pixels possibly interfere our proposed model. Thus, in our following experiments, we adopt 5×5 or second-order block to design our GLRT.

Additionally, let us evaluate the performance of the proposed detector dealing with other interpolation algorithms, such as *bicubic* and *nearest*. The dataset *Org_D_1.0* is used to gain re-sampled images with different re-sampling factors. As Table II illustrates, with increasing the re-sampling factor R, the performance of the detector for classifying re-sampled images with *bicubic* interpolation is improved. Obviously, when $R < 1$, the detector cannot perform very well as the AUC result from the scenario $R > 1$. Furthermore, our detector can also detect a non-linear re-sampled image with *nearest* non-linear interpolation. However, the prerequisite has to be satisfied, that is $R > 1$ (see Table III).

3) Performance over Compressed Format Images: To verify that our proposed detector is capable of resisting against image compression, it is proposed to investigate our test based on a group of new datasets consisting of uncompressed and compressed images. First, we establish the dataset *Org_D_1.0_U* in which 1000 uncompressed images are randomly select-
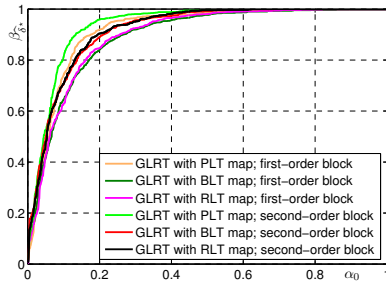
Fig. 13: Illustration of detection power based on different blocks; re-sampling factor $R = 1.1$.

TABLE II: Detection performance (Area Under Curve, AUC) comparison with *bicubic* interpolation. The designed GLRT with three texture weight maps.

R	PLT	BLT	RLT
1.50	1	1	1
1.30	0.98	0.97	0.97
1.10	0.86	0.81	0.82
0.90	0.76	0.71	0.71
0.70	0.77	0.72	0.72
0.50	0.68	0.63	0.65

TABLE III: Detection performance (AUC) comparison with *nearest* interpolation. The designed GLRT with three texture weight maps.

R	PLT	BLT	RLT
1.50	1	1	1
1.30	1	1	1
1.10	1	1	1
0.90	0.49	0.49	0.48
0.70	0.43	0.42	0.42
0.50	0.28	0.28	0.29

ed from Bossbase [28]. Afterwards, images of the dataset *Org_D_1.0_U* are compressed and saved as JPEG format, namely dataset *Org_D_1.0_C*. Let us name those datasets as *Re_D_X_C*, where "C" denotes "Compressed"; "X" denotes the re-sampled factor "R". For instance, dataset *Re_D_1.2_95* represents that images in this dataset are re-sampled using the re-sampling factor "1.2", and compressed with the quality factor 95.

By investigating the effect of once-compressed re-sampled images, let us establish each test dataset consisting of dataset *Org_D_1.0_U* and its re-sampled version with different quality/re-sampling factors. During our experiments, half images of test dataset are re-sampled; another half images are non-resampled. Table IV demonstrates the experimental results. When the re-sampled image saved as JPEG format, our proposed detector can still detect re-sampling forgery. Besides, with decreasing the quality factor, the detection power can be slightly improved. Because JPEG compression probably unavoidably results in re-sampling traces which is generated by DCT transform.

To study the effect of double-compressed re-sampled im-

TABLE IV: Detection performance (true positive rate) comparison of the GLRT with RLT map at the given FAP $\alpha_0 = 0.1$ by detecting re-sampled once-compressed images in test datasets; R represents re-sampling factor, and Q denotes quality factor.

R \ Q	75	80	85	90
1.60	0.99	0.99	0.99	1.00
1.40	0.92	0.90	0.90	0.90
1.20	0.80	0.77	0.72	0.69
Average	0.90	0.89	0.87	0.86

ages, it is proposed to design the test dataset consisting of dataset *Org_D_1.0_C* with the quality factor 90 and its re-sampled version with different quality/re-sampling factors. Let us compare the detection performance of our proposed detectors with three texture weight maps (see Table V). Since the non-resampled images are compressed, the re-sampling traces more or less interferes our detectors. Nevertheless, the numerical results verify that re-sampled images with different quality/re-sampling factors can still be effectively discriminated with acceptable detection accuracy.

TABLE V: Detection performance (true positive rate) comparison at the given FAP $\alpha_0 = 0.15$. The designed GLRT with three texture weight maps, referring to as PLT, BLT, and RLT.

Test dataset	PLT	BLT	RLT
Org_D_1.0_C and *Re_D_1.2_95*	0.78	0.75	0.90
Org_D_1.0_C and *Re_D_1.3_85*	0.90	0.88	0.93
Org_D_1.0_C and *Re_D_1.4_75*	0.96	0.94	0.98
Org_D_1.0_C and *Re_D_1.5_70*	1.00	0.99	1.00
Average	0.91	0.90	0.95

4) Performance against Noise Adding Attack: The main idea behind our proposed algorithm is that the detectors are established based on the statistical distribution of residual noise. Thus, it makes sense that we propose to investigate the detection performance when our adaptive statistical detectors suffer from noise adding attack.

Let us consider two scenarios. In the first scenario, we select all the non-resampled images from Ucid dataset (see [35]). Then, by re-sampling those images and adding the Gaussian-distributed noise, we can acquire re-sampled images with additive noise. It should be noted that each test dataset consists of 1338 non-resampled images without adding noise while 1338 re-sampled images with adding noise. The Gaussian-distributed noise can be represented by $\mathcal{N}(x, y)$, where x denotes expectation and y denotes variance. $\mathcal{N}(0, 0)$ denotes that no Gaussian-distributed noise is added into images. As Table VI illustrates, our detectors attacked by additive noise with small variance perform nearly comparably to (a little worse than) the detectors without suffering the attack. Because the residual noise is extracted among neighboring re-sampled pixels by using the parametric linear model. The linear subtraction operation probably to some extent offsets the disturbance caused by additive noise. However, when we further increase the noise variance, it is unavoidable that

the hand-crafted additive noise affects the linear relationship among neighboring pixels, resulting in the inaccuracy of the established statistical model. Thus, the high detection accuracy cannot be guaranteed.

Additionally, it is proposed to consider the second scenario. We add the Gaussian-distributed noise into all the non-resampled images from Ucid dataset (see [35]). Then, those images with additive noise are re-sampled. We establish each test dataset including 1338 non-resampled images with additive noise and 1338 re-sampled images generated from the images with additive noise. Table VII reports the detection results from three texture weight maps suffering the noise attack with different parameters. It can be observed that with increasing the variance of the additive noise, the performance of our proposed detector is better and better. It should be emphasized that all the detectors dealing with the case of additive noise outperform that of detecting the images without additive noise. When the appropriate amount of noise is added into non-resampled images, the texture complexity degree of the image can be enhanced, leading to that our proposed texture weight maps can more effectively describe the distinguishable features between a non-resampled and re-sampled image (see details in Section III). Therefore, the detection performance is improved.

TABLE VI: Detection performance (AUC) comparison of the GLRT with three maps by detecting re-sampled images with adding the Gaussian-distributed noise.

(a) Detection performance with $R = 1.2$

Noise parameters	PLT	BLT	RLT
$\mathcal{N}(0, 0)$	0.9721	0.9632	0.9628
$\mathcal{N}(0, 1)$	0.9673	0.9514	0.9537
$\mathcal{N}(0, 2)$	0.9629	0.9416	0.9457
$\mathcal{N}(0, 3)$	0.9589	0.9329	0.9385
$\mathcal{N}(0, 4)$	0.9551	0.9245	0.9317
Average	0.9633	0.9427	0.9465

(b) Detection performance with $R = 0.8$

Noise parameters	PLT	BLT	RLT
$\mathcal{N}(0, 0)$	0.8831	0.8502	0.8515
$\mathcal{N}(0, 1)$	0.8815	0.8403	0.8432
$\mathcal{N}(0, 2)$	0.8792	0.8320	0.8364
$\mathcal{N}(0, 3)$	0.8767	0.8242	0.8299
$\mathcal{N}(0, 4)$	0.8743	0.8170	0.8237
Average	0.8790	0.8327	0.8369

5) Performance Comparison with Prior Arts: To compare with some un-supervised prior arts such as algorithms of [11], [16], [18], let us present the detailed detection performance using different re-sampling detectors. In the following experiments, Ucid dataset is still used for establishing our testing datasets. It should be noted that all the re-sampled images are uncompressed with different re-sampling factors.

Table VIII demonstrates the comparison of the detection performance at the given FAP α_0. For the case of re-sampling forgery with $R > 1$ (see Table VIIIa), our proposed detectors

TABLE VII: Detection performance (AUC) comparison of the GLRT with three maps by adding the Gaussian-distributed noise to non-resampled images.

(a) Detection performance with $R = 1.2$

Noise parameters	PLT	BLT	RLT
$\mathcal{N}(0, 0)$	0.9721	0.9632	0.9628
$\mathcal{N}(0, 1)$	0.9741	0.9677	0.9672
$\mathcal{N}(0, 2)$	0.9759	0.9714	0.9705
$\mathcal{N}(0, 3)$	0.9777	0.9744	0.9735
$\mathcal{N}(0, 4)$	0.9793	0.9770	0.9760
Average	0.9758	0.9707	0.9700

(b) Detection performance with $R = 0.8$

Noise parameters	PLT	BLT	RLT
$\mathcal{N}(0, 0)$	0.8831	0.8502	0.8515
$\mathcal{N}(0, 1)$	0.8841	0.8572	0.8581
$\mathcal{N}(0, 2)$	0.8860	0.8629	0.8633
$\mathcal{N}(0, 3)$	0.8880	0.8682	0.8682
$\mathcal{N}(0, 4)$	0.8899	0.8729	0.8725
Average	0.8862	0.8623	0.8627

with three different texture maps outperform other detectors. Moreover, with the very small re-sampling factor such as $R = 1.2$, the detection rate of the GLRT with PLT map nearly approaches to 1, which performs better than other prior arts. When the re-sampling detector $R < 1$ (see Table VIIIb), the GLRT with PLT map still performs better than other detectors. In fact, due to the linear correlation among pixels is somewhat damaged caused by down-sampling operation, the detection accuracy of our detectors with $R < 1$ is worse than its counterpart with $R > 1$.

Afterwards, it is proposed to compare our test with a typical supervised algorithm of [25]. When the inspected image is compressed with the quality factor 95, the detection rate of [25] dealing with the case of $R = 1.2$ approaches 0.65. However, the detection rate of our proposed GLRT with RLT map can achieve 0.9 (see Table V for details). Therefore, our proposed detector perform more robustly. In addition, when dealing with the case of uncompressed images, our proposed detector perform comparable to the algorithm of [25]. It should be noted that the algorithm of [25] can effectively estimate the re-sampling factor, which is not studied in this context.

Besides, let us compare our detectors with another supervised detector (see [27]). Still, we use Ucid dataset. Note that all 1338 images are compressed with the quality factor 55 after re-sampling process. It should be emphasized that for fair comparison, we establish the same experimental data as the authors of [27] did. Through the comparative experiment (see Table IX), all our proposed GLRTs with three maps perform better than the detector of [27] in the case of low quality factor 55.

In fact, when $R < 1$ (for instance, R equals to 0.8), our detector cannot outperform the algorithm proposed in [20], that is the limitation of our statistical detector dealing with down-sampled images. In [18], 200 images (acquired by one

TABLE VIII: Detection performance (true positive rate) comparison under two hypotheses between $\mathcal{H}_0$ and $\mathcal{H}_1$ at the given FAP α_0.

(a) Re-sampling detection performance with $R > 1$ and $\alpha_0 = 0.1$

R	GLRT with PLT map	GLRT with BLT map	GLRT with RLT map	Detector [11]	Fixed pattern [18]	EM algorithm [16]
1.50	1.00	1.00	1.00	0.98	0.91	0.89
1.40	1.00	1.00	1.00	0.91	0.80	0.79
1.30	1.00	1.00	1.00	0.81	0.73	0.70
1.20	0.98	0.92	0.92	0.69	0.62	0.62
1.10	0.84	0.72	0.73	0.56	0.51	0.50
Average	**0.96**	**0.93**	**0.93**	0.79	0.71	0.70

(b) Re-sampling detection performance with $R < 1$ and $\alpha_0 = 0.15$

R	GLRT with PLT map	GLRT with BLT map	GLRT with RLT map	Detector [11]	Fixed pattern [18]	EM algorithm [16]
0.95	0.78	0.65	0.67	0.56	0.65	0.64
0.90	0.79	0.65	0.65	0.55	0.66	0.63
0.85	0.79	0.65	0.65	0.55	0.67	0.63
0.80	0.81	0.66	0.68	0.56	0.68	0.62
Average	**0.79**	0.65	0.66	0.56	0.67	0.63

TABLE IX: Detection performance (AUC) comparison between our proposed detectors and the algorithm of [27] by detecting re-sampled compressed images with quality factor 55; R represents re-sampling factor.

R	PLT	BLT	RLT	Detector [27]
1.60	0.99	0.99	0.99	0.88
1.40	0.98	0.98	0.97	0.88
1.20	0.97	0.96	0.95	0.81
Average	**0.98**	**0.98**	**0.97**	0.86

camera device) consists of the testing dataset while ours use 1338 images from Ucid benchmark dataset, which leading to that the results of detection cannot be guaranteed to remain same.

VII. CONCLUSIONS AND DISCUSSIONS

This paper investigates the problem of classifying between non-resampled and re-sampled images. In most prior studies of re-sampling forgery authentication, few literature mainly focuses on establishing the detector based on statistical models and hypothesis testing theory. In this context, it is proposed to characterize the noise extracted from a re-sampled image using the Gaussian distribution while the noise of a non-resampled image is modeled by the Uniform distribution. More importantly, three texture weight maps are designed to remarkably improve the detection power of the GLRT; we specifically establish the framework of the LRT based on the proposed models, and theoretically verify the effectiveness of the proposed model-based statistical detector. Finally, our proposed practical detector performs relevantly better than some prior arts involving some un-supervised ([11], [16], [18]) and supervised algorithms ([25], [27]). Furthermore, our proposed adaptive algorithm performs its robustness when dealing with the cases of JPEG compression and additive noise attack. In addition, we do not arbitrarily give the threshold (or

FAP) in the practical classification. In fact, we need specify the FAP according to the number of tested images. For instance, to deal with a large scale of images, we usually select a considerably small FAP while a large FAP is adopted in the case of authenticating a few of images.

The main limitations of this paper are as follows: the statistical model for non-resampled images is not very accurate; the re-sampled image with a large scale of smooth areas cannot be effectively identified. Fig. 14 illustrates some images with a large scale of smooth areas selected from Ucid dataset, where the re-sampled images with $R = 1.3$ cannot be effectively detected using our proposed algorithm. By observation, in the case that at least 70% areas of the images are considerably smooth, our detectors become invalid. For Fig. 14a, the smooth areas nearly occupy the whole image. Note that with increasing the value of R, the impact from the smooth areas can be weakened while the detection power can be improved (see Fig. 11). In fact, when dealing with an image owning the homogeneous pixel intensity such as an overexposed image, both our algorithm and some prior arts hardly perform effectively. Besides, the problem of how to improve the detection rate for authenticating re-sampled images with $R < 1$ remains open.

APPENDIX A
EXPECTATION AND VARIANCE OF LR $\Lambda(\omega_l)$

In this appendix, let us to extend the specific calculation of the expectation and variance of LR $\Lambda(\omega_l)$. First, let us give the pdf of the proposed model in our practical context under two hypotheses. Under hypothesis H_0, the Uniform model is formulated as:

$$\mathcal{P}_{\boldsymbol{\theta}_0}[\omega_l] = \begin{cases} \dfrac{1}{b-a} & \text{if } a \leq \omega_l \leq b, \\ 0 & \text{if else.} \end{cases} \tag{30}$$

where parameter $\boldsymbol{\theta}_0 = (a, b)$ denote the range of non-zero value from its pdf. It is very interesting that its pdf is

| (a) | (b) | (c) | (d) | (e) | (f) |

Fig. 14: Illustration of the inspected images with incorrect detection. When re-sampling these images with a large scale of smooth areas, our proposed adaptive detectors cannot correctly distinguish between these non-resampled images and the re-sampled ones.

independent of random variables. In this practical context, we only study the probability within the range from a to b. To this end, the expectation $E_{\mathcal{H}_0}[\omega_l]$ and variance $V_{\mathcal{H}_0}[\omega_l]$ of random variables can be respectively expressed as: $\frac{a+b}{2}$ and $\frac{(b-a)^2}{12}$. Then under hypothesis $\mathcal{H}_1$, let us write the pdf of the Gaussian model as:

$$\mathcal{P}_{\boldsymbol{\theta}_1}[\omega_l] = \frac{1}{\sqrt{2\pi\sigma^2}} \exp \frac{\omega_l^2}{-2\sigma^2} \qquad (31)$$

where parameter $\boldsymbol{\theta}_0 = (0, \sigma^2)$ denote its expectation and variance. That is, $E_{\mathcal{H}_1}[\omega_l] = 0$ and $V_{\mathcal{H}_1}[\omega_l] = \sigma^2$. Thus, the LR $\Lambda(\omega_l)$ (see Eq. (13)) for one observation can be re-written as:

$$\Lambda(\omega_l) = \log\left(\frac{b-a}{\sqrt{2\pi\sigma^2}}\right) - \frac{\omega_l^2}{2\sigma^2} \qquad (32)$$

In virtue of Eq. (32), under hypothesis $\mathcal{H}_1$ one can calculate the expectation and variance of LR $\Lambda(\omega_l)$ by using:

$$E_{\mathcal{H}_1}\left(\Lambda(\omega_l)\right) = \log\left(\frac{b-a}{\sqrt{2\pi\sigma^2}}\right) - \frac{1}{2} \qquad (33)$$

$$V_{\mathcal{H}_1}\left(\Lambda(\omega_l)\right) = \frac{1}{2} \qquad (34)$$

Then under hypothesis $\mathcal{H}_0$, the expectation of LR $\Lambda(\omega_l)$ can be formulated by:

$$E_{\mathcal{H}_0}\left(\Lambda(\omega_l)\right) = \log\left(\frac{b-a}{\sqrt{2\pi\sigma^2}}\right) - \frac{E_{\mathcal{H}_0}(\omega_l^2)}{2\sigma^2} \qquad (35)$$

where $E_{\mathcal{H}_0}(\omega_l^2) = \frac{a^2+ab+b^2}{3}$. The variance of LR $\Lambda(\omega_l)$ can be expressed as:

$$V_{\mathcal{H}_0}\left(\Lambda(\omega_l)\right) = \frac{V_{\mathcal{H}_0}(\omega_l^2)}{4\sigma^4} \qquad (36)$$

where $V_{\mathcal{H}_0}(\omega_l^2) = \frac{4u_{ab}^4}{45}$, $u_{ab} = \max\{|a|, |b|\}$, $|\cdot|$ denotes the absolute value.

REFERENCES

[1] F. Technologies, "Photo tampering throughout history," http://pth.izitru.com.
[2] H. T. Sencar and N. Memon, *Digital image forensics: There is more to a picture than meets the eye.* Springer, 2012.
[3] T. H. Thai, R. Cogranne, and F. Retraint, "Camera model identification based on the heteroscedastic noise model," *IEEE Transactions on Image Processing*, vol. 23, no. 1, pp. 250–263, 2014.
[4] T. Qiao, F. Retraint, R. Cogranne, and T. H. Thai, "Source camera device identification based on raw images," in *Image Processing (ICIP), 2015 IEEE International Conference on*. IEEE, 2015, pp. 3812–3816.
[5] ——, "Individual camera device identification from jpeg images," *Signal Processing: Image Communication*, vol. 52, pp. 74–86, 2017.
[6] D. Valsesia, G. Coluccia, T. Bianchi, and E. Magli, "Large-scale image retrieval based on compressed camera identification," *IEEE Transactions on Multimedia*, vol. 17, no. 9, pp. 1439–1449, 2015.
[7] J. Li, X. Li, B. Yang, and X. Sun, "Segmentation-based image copy-move forgery detection scheme," *IEEE Transactions on Information Forensics and Security*, vol. 10, no. 3, pp. 507–518, 2015.
[8] L. Su, C. Li, Y. Lai, and J. Yang, "A fast forgery detection algorithm based on exponential-fourier moments for video region duplication," *IEEE Transactions on Multimedia*, vol. 20, no. 4, pp. 825–840, 2018.
[9] X. Zhao, S. Wang, S. Li, and J. Li, "Passive image-splicing detection by a 2-d noncausal markov model," *IEEE Transactions on Circuits and Systems for Video Technology*, vol. 25, no. 2, pp. 185–199, 2015.
[10] C. Li, Q. Ma, L. Xiao, M. Li, and A. Zhang, "Image splicing detection based on markov features in qdct domain," *Neurocomputing*, vol. 228, pp. 29–36, 2017.
[11] T. Qiao, A. Zhu, and F. Retraint, "Exposing image resampling forgery by using linear parametric model," *Multimedia Tools and Applications*, vol. 77, no. 2, pp. 1501–1523, 2018.
[12] X. Feng, I. J. Cox, and G. Doerr, "Normalized energy density-based forensic detection of resampled images," *IEEE Transactions on Multimedia*, vol. 14, no. 3, pp. 536–545, 2012.
[13] X. Lin, J. Liu, and X. Kang, "Audio recapture detection with convolutional neural networks," *IEEE Transactions on Multimedia*, vol. 18, no. 8, pp. 1480–1487, 2016.
[14] Z. Jin, J. Cao, Y. Zhang, J. Zhou, and Q. Tian, "Novel visual and statistical image features for microblogs news verification," *IEEE transactions on Multimedia*, vol. 19, no. 3, pp. 598–608, 2017.
[15] H. Li, W. Luo, X. Qiu, and J. Huang, "Identification of various image operations using residual-based features," *IEEE Transactions on Circuits and Systems for Video Technology*, 2016.
[16] A. C. Popescu and H. Farid, "Exposing digital forgeries by detecting traces of resampling," *IEEE Transactions on Signal Processing*, vol. 53, no. 2, pp. 758–767, 2005.
[17] A. C. Gallagher, "Detection of linear and cubic interpolation in jpeg compressed images," in *Computer and Robot Vision, 2005. Proceedings. The 2nd Canadian Conference on*. IEEE, 2005, pp. 65–72.
[18] M. Kirchner, "Fast and reliable resampling detection by spectral analysis of fixed linear predictor residue," in *Proceedings of the 10th ACM workshop on Multimedia and security*. ACM, 2008, pp. 11–20.
[19] B. Mahdian and S. Saic, "Blind authentication using periodic properties of interpolation," *IEEE Transactions on Information Forensics and Security*, vol. 3, no. 3, pp. 529–538, 2008.

[20] M. Kirchner, "Linear row and column predictors for the analysis of resized images," in *Proceedings of the 12th ACM workshop on Multimedia and security*. ACM, 2010, pp. 13–18.

[21] D. Vázquez-Padín, C. Mosquera, and F. Pérez-González, "Two-dimensional statistical test for the presence of almost cyclostationarity on images," in *Image Processing (ICIP), 2010 17th IEEE International Conference on*. IEEE, 2010, pp. 1745–1748.

[22] D. Vazquez-Padin, P. Comesana, and F. Perez-Gonzalez, "Set-membership identification of resampled signals," in *Information Forensics and Security (WIFS), 2013 IEEE International Workshop on*. IEEE, 2013, pp. 150–155.

[23] D. Vazquez-Padin, F. Pérez-González, and P. Comesana-Alfaro, "A random matrix approach to the forensic analysis of upscaled images," *IEEE Transactions on Information Forensics and Security*, vol. 12, no. 9, pp. 2115–2130, 2017.

[24] C. Pasquini and R. Böhme, "Information-theoretic bounds of resampling forensics: New evidence for traces beyond cyclostationarity," in *Proceedings of the 5th ACM Workshop on Information Hiding and Multimedia Security*. ACM, 2017, pp. 3–14.

[25] N. Zhu, C. Deng, and X. Gao, "A learning-to-rank approach for image scaling factor estimation," *Neurocomputing*, vol. 204, pp. 33–40, 2016.

[26] S.-J. Ryu and H.-K. Lee, "Estimation of linear transformation by analyzing the periodicity of interpolation," *Pattern Recognition Letters*, vol. 36, pp. 89–99, 2014.

[27] Y. Su, X. Jin, C. Zhang, and Y. Chen, "Hierarchical image resampling detection based on blind deconvolution," *Journal of Visual Communication and Image Representation*, vol. 48, pp. 480–490, 2017.

[28] P. Bas, T. Filler, and T. Pevnỳ, "Break our steganographic system? the ins and outs of organizing boss," in *Information Hiding*. Springer, 2011, pp. 59–70.

[29] P. L. Correia and F. Pereira, "Objective evaluation of video segmentation quality," *IEEE Transactions on Image Processing*, vol. 12, no. 2, pp. 186–200, 2003.

[30] N. Otsu, "A threshold selection method from gray-level histograms," *Automatica*, vol. 11, no. 285-296, pp. 23–27, 1975.

[31] E. L. Lehmann and J. P. Romano, *Testing statistical hypotheses*. Germany: Springer, 2006.

[32] T. Qiao, F. Retraint, R. Cogranne, and C. Zitzmann, "Steganalysis of jsteg algorithm using hypothesis testing theory," *EURASIP Journal on Information Security*, vol. 2015, no. 1, p. 2, 2015.

[33] T. Qiao, C. Zitzmann, F. Retraint, and R. Cogranne, "Statistical detection of jsteg steganography using hypothesis testing theory," in *Image Processing (ICIP), 2014 IEEE International Conference on*. IEEE, 2014, pp. 5517–5521.

[34] T. Qiao, C. Zitzmann, R. Cogranne, and F. Retraint, "Detection of JSteg algorithm using hypothesis testing theory and a statistical model with nuisance parameters," in *Proceedings of the 2nd ACM workshop on Information hiding and multimedia security*. ACM, 2014, pp. 3–13.

[35] G. Schaefer and M. Stich, "Ucid: an uncompressed color image database," in *Electronic Imaging 2004*. International Society for Optics and Photonics, 2003, pp. 472–480.